

2023

Section: Chemistry

Green Synthesis Of Zinc Oxide Nanoparticles: Characterization, Organic Dye Degradation And Evaluation Of Their Antibacterial Activity

Mona Khamis

Department of Chemistry, Faculty of Science, Al-Azhar University, Assiut 71524, Egypt

Gamal A. Gouda

Department of Chemistry, Faculty of Science, Al-Azhar University, Assiut 71524, Egypt,
ggouda73@azhar.edu.eg

Adham M. Nagiub

Department of Chemistry, Faculty of Science, Al-Azhar University, Assiut 71524, Egypt

Follow this and additional works at: <https://absb.researchcommons.org/journal>

How to Cite This Article

Khamis, Mona; Gouda, Gamal A.; and Nagiub, Adham M. (2023) "Green Synthesis Of Zinc Oxide Nanoparticles: Characterization, Organic Dye Degradation And Evaluation Of Their Antibacterial Activity," *Al-Azhar Bulletin of Science*: Vol. 34: Iss. 2, Article 7.

DOI: <https://doi.org/10.58675/2636-3305.1650>

This Original Article is brought to you for free and open access by Al-Azhar Bulletin of Science. It has been accepted for inclusion in Al-Azhar Bulletin of Science by an authorized editor of Al-Azhar Bulletin of Science. For more information, please contact kh_Mekheimer@azhar.edu.eg.

Green Synthesis of Zinc Oxide Nanoparticles: Characterization, Organic Dye Degradation and Evaluation of Their Antibacterial Activity

Mona Khamis, Gamal A. Gouda*, Adham M. Naguib

Department of Chemistry, Faculty of Science, Al-Azhar University, Assiut, Egypt

Abstract

The aim of this work is the green synthesis of zinc oxide nanoparticles (ZnO NPs) via red onion extract. The ZnO NPs wurtzite hexagonal structure was identified through radiography diffraction (XRD) analysis, with an average crystallite size of 8.13 nm. The capping and stabilization of ZnO NPs biosynthesis were supported by an analysis of fourier transform infrared (FT-IR). The absorption peak at 374 nm with an energy bandgap of 3.32 eV was discovered via ultraviolet–vision (UV–Vis) analysis. A morphological study was done by scanning electron microscopy (SEM) and transmission electron microscope (TEM) techniques and showed that spherical ZnO NPs with diameters ranging from 2.83 to 15.35 nm had formed. Using EDS, it was possible to identify the high purity, intensity, and crystalline width of zinc and oxygen. The removal rates of methylene blue (MB) by photocatalysis and adsorption were compared utilizing ZnO NPs. Under sunlight, the photodegradation of MB 10 mg/L has been examined. It was found that maximum decolorization efficiency happened after 120 min and a dose of 25 mg of ZnO NPs. The adsorption capacity (q_m) was calculated by the Langmuir equation to be 10.8 mg/g. The kinetic analysis suggests the pseudo-second-order model was followed during MB adsorption via the NPs. The findings showed that the photocatalytic and adsorption approaches removed the dye up to 95.2% more efficiently than in earlier research. ZnO NPs exhibited better antibacterial action against *Escherichia coli* than *Staphylococcus aureus* bacteria when compared with a common antibiotic like *Ciprofloxacin*.

Keywords: Antimicrobial activity, Organic dye degradation, Zinc oxide nanoparticle

1. Introduction

Green nanotechnology is used to create nanoparticles that are more environmentally sustainable and to process nanomaterials in safe settings [1]. The prospective benefits of this sector, which include eco-friendliness, usability, and very significant energy savings [2], have drawn attention. Large-scale chemical and physical processes are used to create nanomaterials, but their use and disposal raise questions regarding potential environmental effects. As a result, biogenic synthesis, sometimes referred to as a ‘green synthesis strategy,’ offers a practical basis for the long-term and sustainable manufacture of nanomaterials [3–5].

The two primary types of biosynthesis are mediated by microorganisms and plants, with the latter attracting more attention due to its accessibility, cost, and convenience of use [6]. Recently, a biological zinc oxide nanoparticles (ZnO NPs) synthesis based on plant extracts has been established, and it offers several advantages over chemical and physical ways, including lower costs, simpler handling, nontoxicity, and environmental friendliness. ZnO NPs has previously been produced using a variety of plants, including *Citrus sinensis*, *Moringa oleifera*, Oak fruit, and *Brassica oleracea* [7]. The employing of ZnO NPs in several applications, including ultraviolet (UV) absorption [8], antibacterial treatment [9], photocatalysts [10], solar cells [11], luminous

Received 9 July 2023; revised 31 July 2023; accepted 2 August 2023.
Available online 16 October 2023

* Corresponding author at: Department of Chemistry, Faculty of Science, Al-Azhar University, Assiut Branch, Assiut 71524, Egypt. Fax: 02 (088) 2148093. E-mail address: ggouda73@azhar.edu.eg (G.A. Gouda).

<https://doi.org/10.58675/2636-3305.1650>

2636-3305/© 2023, The Authors. Published by Al-Azhar university, Faculty of science. This is an open access article under the CC BY-NC-ND 4.0 Licence (<https://creativecommons.org/licenses/by-nc-nd/4.0/>).

materials [9], and drug-delivery [12], has generated significant attention. Due to its wide band gap energy, remarkable optical features, increased electrophobicity, nontoxicity, and antibacterial capabilities, ZnO NPs are one of the most promising photocatalysts [13]. Furthermore, it is asserted that the production of ZnO NPs is substantially less expensive than that of TiO₂ and Al₂O₃ nanoparticles [14]. Zinc oxide has a higher exciton binding energy than certain other often researched photocatalytic semiconductors, such as TiO₂ and SnO₂ [15], as well as a direct band gap semiconductor (3.37 eV), which enables it to absorb visible light more effectively [16]. Many industries employ synthetic dyes extensively, but when they are released into the environment untreated, they cause major health problems and environmental damage. These contaminants must be removed from industrial effluent because they are inherently toxic and have a negative impact on aquatic life. The dyes have been removed from aquatic environments using a number of techniques, including chemical oxidation, photocatalysis, and adsorption [17]. One of the best techniques for eliminating wastewater from dye-related pollution is adsorption. Additionally, photocatalyst-based dye degradation include a high catalytic efficiency, cheap cost, and quick conversion of various contaminants into innocuous chemicals [18–20]. In addition, it can be employed successfully when exposed to solar light by using the appropriate photocatalytic materials [21]. It has been demonstrated that semiconductors outperform other material systems in the photocatalytic oxidation of dyes [22,23]. Moreover, it has been shown that these materials work well for dye adsorption and are appropriate for water splitting reactions that produce hydrogen and oxygen [24].

The surface of ZnO has a negative charge that is perfect for electrostatic interaction and the adsorption of methylene blue (MB) [25]. An effective antioxidant and anticancer is the onion (*Allium cepa*) [26]. In GC–MS analysis of red onion extract was which stated in Momoh et al. study [27], they referred to the bioactive molecules such as polyphenols, flavonoids, terpenoids, alkaloids, and tannins. The extract works as a powerful chelating agent to help with the formation of ZnO NPs, and capping/stabilizing process (i.e. quercetin) because it contains anthocyanins (derivatives of cyanidin) and flavanols [28].

This study highlighted the use of onion extract as a safe way of producing ZnO NPs. Then, using a variety of approaches, physicochemical analysis was used to confirm the nanoscale biosynthesis of ZnO NPs. The effectiveness of MB dye removal from

water by photocatalytic degradation and adsorption by ZnO NPs was researched. Furthermore, research on the antibacterial capacities of *Ciprofloxacin* and ZnO NPs against of some bacteria were done.

2. Experimental

2.1. Chemicals and reagents

Analytical-grade compounds were employed in the current investigation. Acetonitrile, ethanol, HCl with a purity of 37%, HPLC grade from LOBA CHEMIE, NaOH (Scharlau, Spain), 99% pure ZnSO₄, and NH₄OH with a concentration of 35% (Merck, UK). *Ciprofloxacin* was kindly donated by Organo for Pharmaceutical and Chemical Industries in Obour City, Egypt, serving as an antibacterial standard.

2.2. Synthesis of ZnO NPs

With use of distilled water, the red onions were meticulously washed before being shade-dried for about 100 g at room temperature. A glass tank containing the dried onions is filled with 50% aqueous ethanol and let to soak for 2.5 days. After the solid material has been eliminated and filtered, any leftover solids are subsequently eliminated using Whatman filters. Until it was time to employ the filtrate for the biosynthesis of ZnO NPs, it was kept at 25 °C. At 60 °C, 100 mL of the onion extract solution was gradually added to 60 mM of aqueous ZnSO₄. The pH is adjusted to 10.5 with a 25% ammonia solution while the mixture is kept at 60 °C and continuously stirred. After the addition, the solution was allowed to react for an hour, at which point a brown precipitate could be seen. After being allowed to rest for 24 h, the precipitate was rinsed with double-distilled water and ethanol, and then it was separated by centrifuging at 5000 rpm for 20 min. At 60 °C, the material was dried for 6 h. ZnO NPs separated precipitate was calcined for 2 h at 300 and 400 °C.

2.3. Characterizations

To analyze the ZnO NPs crystal phase data, the German Electric Muffle Furnace ST-1200°C-666 was used to produce solid ZnO at the nanoscale. Radiography diffractometer (Philips, PW-1710) was used to determine the ZnO NPs diameters, which ranged from 10 to 80° in 2θ. The size of ZnO NPs was established using scherrers formula and the lattice parameters [29], listed in Table 1 Eqs. (1)–(10).

Table 1. The lattice parameters were used to identify the size of zinc oxide nanoparticles.

Equation	No.	Parameter indications
$D = \frac{K\lambda}{\beta \cos \theta}$	(1)	D: size of crystallite K: constant λ : wavelength θ : Bragg angle β : full width
$a = \frac{\lambda}{\sqrt{3} \sin \theta_{(100)}}$	(2)	c/a: values confirmed that the prepared NPs were crystalline in nature
$c = \frac{\lambda}{\sin \theta_{(002)}}$	(3)	
$d = \frac{\lambda}{2 \sin \theta}$	(4)	d: spacing of sample
$V = \frac{\sqrt{3}}{2} a^2 c$	(5)	V: unit cell volume (\AA^3)
$D^x = \frac{16M}{Na^2}$	(6)	D ^x : density M: molecular mass N: Avogadro's number (6.0223×10^{23})
$\delta = \frac{1}{D^2}$	(7)	δ : the dislocation density
$\varepsilon = \frac{\beta \cos \theta}{4}$	(8)	ε : micro strain
$\sigma_{stress} = \varepsilon E$	(9)	σ : stress E: the elastic constant
$SF = \left[\frac{2\pi^2}{45\sqrt{3} \tan \theta} \right]$	(10)	SF: stress, and stacking fault

Scanning electron microscopy (SEM; QUANTA-FEG-250 with energy dispersive X-ray EDX) and transmission electron microscope (TEM; JEM-100CXII, at a voltage of 80 kV) was evaluate ZnO NPs surface morphology. Elemental analysis of the as-prepared NPs was assessed using EDX analysis. The fourier transform infrared (FT-IR) spectra of prepared NPs were captured by a Thermo Fishers Nicolet iS10 FT-IR spectrometer. UV–Vis absorption spectra were measured using a PerkinElmer Spectrophotometer (Lambda 750 UV/Vis/NIR) in 200–900 nm range. Employ equation (11) from the Tauc relationship to determine the semiconductors electronic band gap [30].

$$(\alpha h\nu)^n = A(h\nu - E_g) \quad (11)$$

where α is coefficient of absorption, h is the Planck's constant, ν is the photon frequency, and E_g is the optical band gap. On the Hitachi (F-7100) fluorescence spectrophotometer, photoluminescence (PL) measurements were made.

2.4. Contaminated methylene blue-water treatment by batch adsorption study

In order to identify the factors impacting pH, adsorbent dosage, contact time, initial concentration, and temperature on the adsorption process, all the parameters against the variable parameter under specific research were fixed for the tested range. Using ordinary acid and alkali, the dye removal efficiency method was conducted at room temperature with pH values ranging from 2 to 10. A range of dye doses between 5 and 40 mg/L were used in the adsorption analysis because ZnO NPs were most successful in removing dye at pH 7.8. The adsorption study was carried out employing a consistent quantity of ZnO NPs to known concentrations of different MB solutions in an agitated beaker for 60 min The adsorbent was separated using a centrifuge (10 000 rpm for 20 min) to get rid of the suspended particles. The remaining MB dye concentration was measured at 664 nm after carefully transferring the resulting supernatant into a quartz cuvette.

2.4.1. Impact of the pH

At a concentration of MB (10 mg/L) on 0.025 g ZnO NPs at room temperature, the removal of the tested dye, MB, by ZnO NPs at various pH levels (2.0–10.0), was investigated by adding 0.1 M HCl or 0.1 M NaOH [31].

2.4.2. Impact of the ZnO NPs adsorbent dose on removal degrade percentage of dye

As a consequence, various ZnO NP doses (0.015–0.035 g) were applied while keeping the MB

Table 2. The isotherm models for methylene blue removal onto zinc oxide nanoparticles adsorbent.

The model	Equation	No.	Definition
Langmuir model [22]	$C_e q_e = (1/q_L K_L) + (1/q_L) C_e$ $R_L = 1/(1+K_L C_{max})$	(14) (15)	q_L is the adsorption capacity of ZnO NPs (mg/g), K_L is adsorption constant of Langmuir energy (L/mg), R_L is the separation factor, C_{max} is initial MB concentration (mg/L).
Freundlich model [32]	$\log q_e = \log K_F + (1/n) \log C_e$	(16)	K_F is adsorption capacity of Freundlich (mg/g), n is the Freundlich constant.
Temkin model [33]	$q_e = B_T \ln A_T + B_T \ln C_e$ $b_T = RT/B_T$	(17) (18)	A_T : binding constant (L/mg), B_T : Temkin adsorption constant (KJ/mol), R : gas constant (8.314 J/mol K), T : absolute temperature, b_T : adsorption process constant.
Dubinin-Radushkevich (D-R) model [33,34]	$\ln q_e = \ln q_m - \beta \epsilon^2$ $\epsilon = RT(1 + 1/C_e)$ $E_D = (-2 \beta)^{-1/2}$	(19) (20) (21)	q_m : D-R adsorption capacity of ZnO NPs (mg/g), β : coefficient related to the mean free energy, ϵ : Polanyi potential, E_D : adsorption energy (kJ/mol)

Table 3. The kinetic models (Eqs. (22)–(25)) were used in evaluating the methylene blue adsorption process.

Model name	Equation	No.	Definition
Pseudo-first order model [33]	$\log (q_e - q_t) = \log q_e - (K_1/2.303)t$	(22)	q_e : amount of MB adsorbed (mg/g) at equilibrium, q_t : amount of MB adsorbed (mg/g) at a predetermined time interval t (min), K_1 : rate constant (min^{-1}).
Pseudo-second order model [35]:	$(t/q_t) = 1/(K_2 q_e^2) + (1/q_e)t$	(23)	K_2 : Rate constant (g/mg min).
Elovich model [36]		(24)	B is constant related to the activation energy for chemisorption (g/mg), α is initial sorption rate constant (mg/g min).
Weber's and Moris's intraparticle diffusion model [37]	$q_t = C + K_{int} (t)^{1/2}$	(25)	K_{int} is intraparticle rate constant ($\text{mg/g min}^{1/2}$), C is value gives information about the boundary thickness.

concentration at 10 mg/L. According to equations 12 and 13 [14], the percentage of photocatalytic degradation and the adsorption experiment were initially carried out to obtain the pH conditions that would result in the largest elimination percentage of MB.

$$\text{Photocatalytic degradation}(\%) = (C_0 - C_e) / C_0 \times 100 \quad (12)$$

$$\text{Adsorbed amount } q_e = (C_0 - C_e)V / m \quad (13)$$

where C_0 is initial concentrations of MB (mg/L), C_e : equilibrium concentration of MB (mg/L), q_e : adsorbed amount of MB (mg/g), V : volume of the MB (mL), and m is mass ZnO NPs (mg).

2.4.3. Isothermal study and impact of the adsorbate MB concentration

The following steps have been taken in order to obtain the practical isothermal kind of adsorption process. With stirring at 240 rpm for 60 min, different 25 mL of the MB adsorbate concentrations of 5–40 mg/L at pH 7.8, and 0.025 g/L of NPs were used. In Table 2, the following isotherm models were used to analyze the results (Eqs. (14)–(21)).

2.4.4. Kinetic modes

Four different kinetic models were being applied to assess the kinetic data to find the best convenient fitted model describing the kinetic mechanism of the methylene blue adsorption onto the surfaces of the ZnO NPs (Table 3).

2.5. Contaminated methylene blue-water treatment by photocatalytic degradation

A model pollutant dye MB was degraded in a solution at a concentration of 10 mg/L in order to assess the ability to ZnO NPs as photocatalysts. The sun served as the study's illumination source. As a consequence, 20 mL of dye solution and 25 mg of ZnO NPs were added to a glass beaker. To help in achieving adsorption equilibrium, the setup was

stirred for 60 min in a fully dark room. The stirrer and the complete contraption were then relocated outside into an area with direct sunshine. When MB was exposed to radiation for periods of 30, 60, 90, and 120 min, the photodegradation of MB was detected. This was done by using a UV–Vis spectrophotometer to measure the intensity of MB absorption peak at 664 nm [38].

2.6. Antimicrobial activity

In the current work, antimicrobial efficacy of biosynthetic ZnO NPs against various microbes was investigated using the well diffusion method. The microorganisms used for the antibacterial activity were *Escherichia coli* ATCC 25922, *Salmonella typhimurium* ATCC 14028, *Staphylococcus aureus* ATCC 25923, and *Enterococcus faecalis* ATCC 29212. *Ciprofloxacin* was the antibacterial agent applied as a positive control. The four distinct ZnO NPs concentrations 225, 250, 275, and 300 $\mu\text{g/mL}$ were made. All the bacteria were tested using different concentrations in dimethyl sulfoxide (DMSO) in a 25 μL volume. The experiments were next conducted using *Ciprofloxacin* as a positive control (275 $\mu\text{g/mL}$), and their results were compared with those obtained using an onion extract and DMSO as a negative control. Each plates zone of inhibition was quantified, and the experiment was run three times.

2.6.1. Preparation of culture strains

A nutrient broth subculture was used to create the pure cultures, which were then incubated at 37 °C overnight for 24 h. The cultures were diluted in the same broth until they had 10^{-3} cfu/mL of concentration. In order to produce the plates, 15 mL of nutritional agar, 1 mL of each diluted culture, and the drilling of wells with sterile pipette tips were required. We moved and added 25 μL of each ZnO NP concentration (225, 250, 275, and 300 $\mu\text{g/mL}$) to the wells. After being left to stand for diffusion, the plates underwent a 24 h incubation at 37 °C.

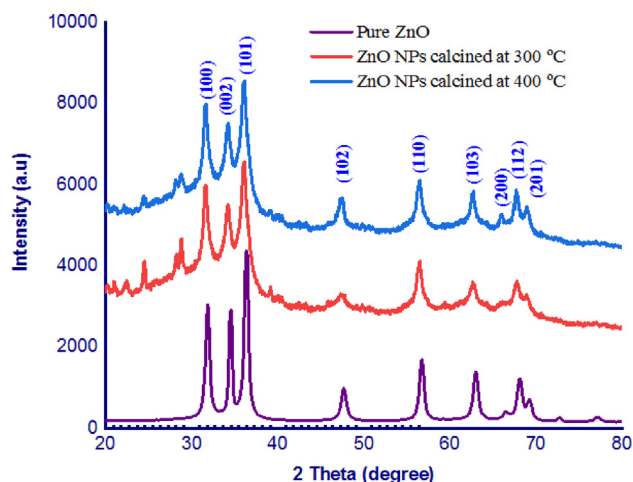


Fig. 1. Radiography diffractogram of pure and biofabricated zinc oxide nanoparticles.

Table 4. Comparison of the radiography diffraction data between standard and fabricated zinc oxide nanoparticles.

Sample	a, Å	c, Å	c/a	V, Å ³	D ^x × 10 ⁴ , kg m ⁻³
Pure ZnO	3.264	5.219	1.598	48.17	6.2133
ZnO NPs	3.2521	5.2221	1.604	47.83	6.2142

3. Results and discussion

3.1. XRD analysis

Figure 1 displays the radiography diffraction (XRD) patterns of pure and fabricated ZnO NPs that were calcined at 300 °C and 400 °C for 2 h. Using x-ray and infrared analyses, it found the purity of the ZnO NPs when calcined at 400 °C is better to that of the sample calcined at 300 °C. Diffraction peaks were seen for lattice planes (100), (002), (101), (102), (110), (103), (200), (112), (200), and (201) at 31.61°, 34.19°, 36.11°, 47.32°, 56.49°, 62.67°, 65.85°, 67.77°, and 68.9°, respectively. These peaks confirmed that the hexagonal wurtzite structure had formed with JCPDS card No. 01-079-0208 [39]. The additional diffraction peaks, which were observed at 24.48°, 28.76°, and 40.5°, are considered to be caused by the onion species. The average particle size of ZnO NPs

was found to be 8.13 nm using Debye-estimation Scherrer's, which is in agreement with the results of SEM and TEM [40]. The values are shown in Table 4, and it is decided that ZnO NPs, *d* spacing is comparable to the standard value because all of the peaks *d* values correspond with the literatures referenced data [41]. The *c/a* values confirmed that the prepared NPs were crystalline in nature. The estimated values for *a* and *c* in Table 4, are agreement with the published values (*a* = 3.246 Å, *c* = 5.219 Å), [41]. The findings in Table 5 clearly show that the strain and dislocation density decrease as the crystallite size increases. The modest value (δ) for pure ZnO NPs denotes flawless crystallisation of the ZnO NPs.

3.2. FT-IR analysis

Figure 2 displays the FT-IR spectra of bio-synthesized ZnO NPs made from onion extract. In Fig. 2, O–H_(St) stretching of the alcohol and phenol groups, N–H_(As) stretching of proteins, and adsorbed water all contribute to the peak at 3407 cm⁻¹ [42]. C–H_(As) asymmetric stretching is attributed to the peak at 2927 cm⁻¹. The characteristic peak at 1636 cm⁻¹ is due to the C=O vibrations in the onion extract, which may have helped to create ZnO NPs [43]. ZnO NPs shows similar peaks, however there are small differences in their positions and intensities. However the broad peak at 3319 cm⁻¹, which was previously found in plant extract, was related to O–H or N–H. The bands at 1055 cm⁻¹ represented the C–O_(As) stretching of the carboxylic acid and ester functional groups. Similarities between the spectra of the ZnO NPs and onion extract suggest the existence of bioactive organic groups as reducing agents, which confirmed that these reducing groups were in charge of the fabrication and stabilization of prepared nanoparticles [13]. According to Zn–O_(As) stretching vibration, the new peak at 567 cm⁻¹ was observed. Previous research has noted that the Zn–O group is responsible for the region between 400 and

Table 5. Calculated parameters of standard zinc oxide powder and fabricated zinc oxide nanoparticles.

Miller indices	<i>d</i> spacing (Å)		Particle size <i>D</i> (nm)	$\delta \times 10^{-15}$ (kg m ⁻³)	$\sigma \times 10^8$ (Pa)	$\epsilon \times 10^{-3}$ (kg m ⁻³) ⁻²	SF
	Standard	Calculated					
100	2.8274	2.8283	8.57	1.36	5.57651	3.95497	0.51
002	2.6096	2.6204	5.54	3.26	8.62815	6.11926	0.78
101	2.486	2.4854	6.65	2.26	7.1852	5.09589	0.65
102	1.9176	1.9194	8.0	1.56	5.97022	4.23420	0.54
110	1.6324	1.6277	10.68	0.88	4.47444	3.17336	0.41
103	1.4817	1.4812	6.69	2.24	7.14307	5.06601	0.65
112	1.3839	1.3816	8.83	1.28	5.41107	3.83764	0.49
201	1.3632	1.3617	10.47	0.91	4.56365	3.23663	0.41

Table 6. A comparison of the zinc oxide nanoparticles generated via green chemistry from onion extract and various plant materials.

No.	Plant source	Extract type	Salt name	Size	Reference
1	<i>Garcinia mangostana</i>	Fruit	Zn(NO ₃) ₂ ·6H ₂ O	21 nm	[50]
2	<i>Mussaenda frondosa</i>	Leaf/stem	Zn(CH ₃ COO) ₂ ·2H ₂ O	5–20 nm	[51]
3	<i>Coriandrum sativum</i>	Leaf	Zn(CH ₃ COO) ₂	24 nm	[10]
4	<i>Sambucus ebulus</i>	Leaf	Zn(CH ₃ COO) ₂ ·2H ₂ O	17 nm	[52]
5	<i>C. sinensis</i>	Peel	Zn(NO ₃) ₂	22.6 nm	[53]
6	Oak	Fruit hull	Zn(CH ₃ COO) ₂ ·2H ₂ O	34 nm	[54]
7	<i>Tabernaemontana divaricata</i>	Green leaf	Zn(NO ₃) ₂	20–50 nm	[55]
8	<i>Dolichos lablab</i> L	Leaf	Zn(CH ₃ COO) ₂ ·2H ₂ O	29 nm	[56]
9	<i>Brassica oleracea</i> L. var. <i>italica</i>	Leaves	ZnCl ₂	14–17 nm	[7]
10	<i>Carica papaya</i>	Latex	Zn(NO ₃) ₂	11–26 nm	[57]
11	Betel	Leaves	Zn(CH ₃ COO) ₂	50 nm	[57]
12	<i>Cannabis sativa</i>	Leaf	Zn(CH ₃ COO) ₂	38 nm	[58]
13	<i>Cyanometra ramiflora</i>	Leaf	Zn(CH ₃ COO) ₂	13 nm	[13]
14	<i>Ferulago angulata</i>	—	Zn(CH ₃ COO) ₂ ·2H ₂ O	32–36 nm	[59]
15	Sea buckthorn	Fruit	Zn(NO ₃) ₂ ·6H ₂ O	17.15 nm	[60]
16	<i>Azadirachta indica</i>	Leaves	Zn(NO ₃) ₂	9–38	[57]
17	<i>Chlorella</i>	—	Zn(NO ₃) ₂	20 ± 2.2 nm	[61]
18	Onion extract	Fruit	ZnSO ₄	2.06–15.3 nm	Current study

600 cm⁻¹. It is interesting to note that ZnO NPs are well produced and stable on calcination up to 400 °C, according to the spectra of the samples calcined at 300 and 400 °C.

3.3. Optical characteristics

Figure 3a Displays the UV–visible spectrum of ZnO NPs dispersed in water. The ZnO NPs showed a single absorption peak at 374 nm, which is the characteristic peak for hexagonal wurtzite ZnO and is almost identical to the ZnO NPs made by *Parthenium* leaf [44]. When compared with the absorption peak of bulk ZnO (365 nm), the peak exhibits a red shift of approximately 9 nm. The emergence of shallow levels can be linked to this red shift. Additionally, no other peaks were visible in the spectrum, demonstrating the high purity of the

prepared ZnO NPs. The E_g in the direct transition was determined by extrapolating the linear portion of the plot of (αhν)² against hν (Fig. 3b) and it was found to be in the range (3.32 eV) [45]. It is clear that from the estimated value of the E_g for the direct transition, confirmation of the proposal of the crystallinity nature of the as-biosynthesized ZnO NPs. The photoluminescence spectrum analysis of synthesized ZnO NPs is shown in (Fig. 3c). The explanation given for the blue-green emission bands (excitonic transitions) seen at 428 nm was that the ZnO NPs had innate crystal defects [46].

3.4. Morphology analysis (SEM, TEM and EDX analyses)

Fig. 4 displays the distribution curves, SEM and TEM microscopy of fabricated ZnO NPs calcined 300 and 400 °C for 2 h. The TEM and SEM images of ZnO NPs show that they have a spherical shape and exhibit high aggregation when they are calcined at of 400 °C. The spherical ZnO NPs in Fig. 4 are uniformly aggregated and, according to a study that examined the crystalline size of the NPs using TEM analysis according to reported elsewhere [47–49], range in size from 2.06 to 15.35 nm on average. The synthesized ZnO NPs by onion extract were smaller than those previously reported (Table 6), according to experiment analyses. The distributions curves shows that the size of the ZnO NPs particles ranged from 1 to 20 nm, and average size of 9.01 nm.

The elemental composition of the biosynthesized ZnO NPs was determined using EDX analysis. The sample created using the aforementioned method has pure ZnO phases, according to the energy dispersive spectra of the samples acquired from the

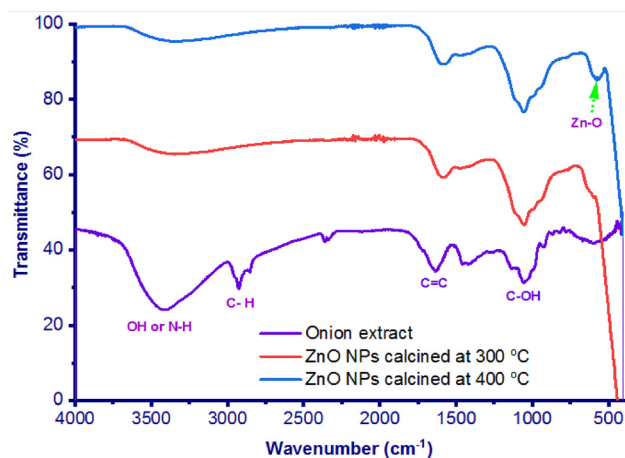


Fig. 2. FT-IR spectra of onion extract and as-biofabricated zinc oxide nanoparticles.

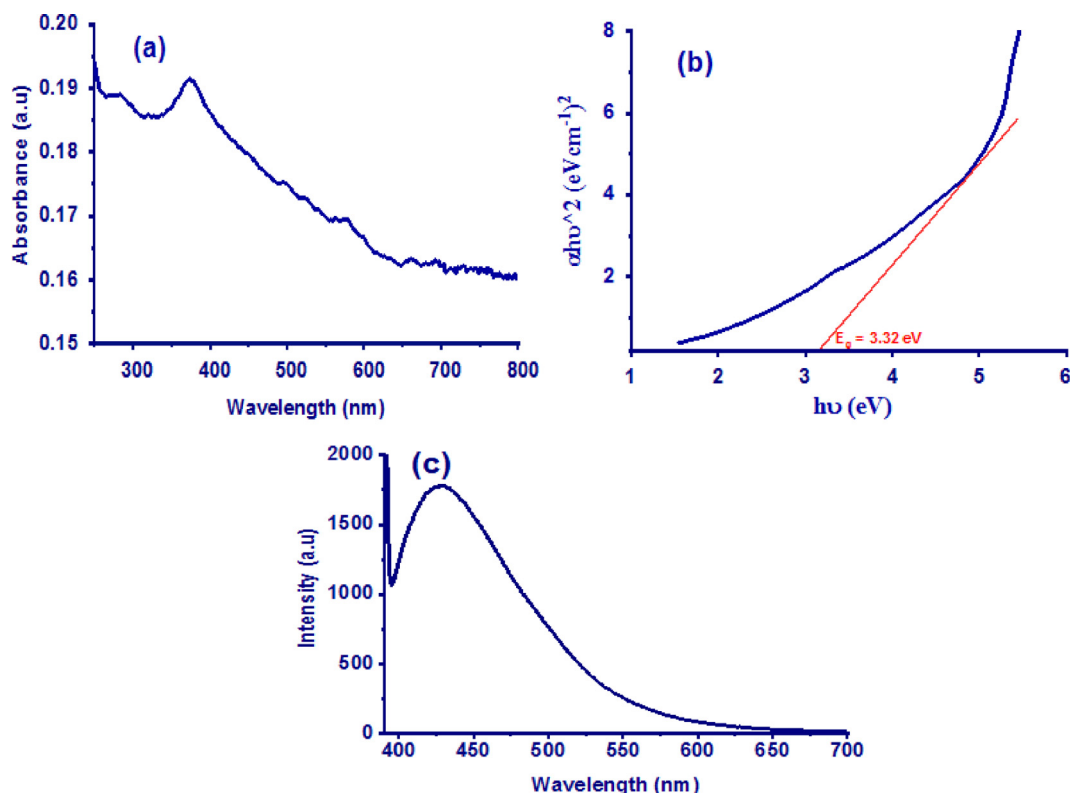


Fig. 3. UV–vis absorption (a), the direct bandgap plots of $(\alpha h\nu)^2$ as a function of photon energy $h\nu$ (b) and PL spectra (c) of zinc oxide nanoparticles.

SEM-EDS analysis. The EDX confirms the existence of zinc and oxygen signals in ZnO NPs, as seen in Fig. 5. The sample analysis revealed that they have a weight-based composition of 71.33% Zn and 15.13 O, indicating that the produced ZnO NPs are in their purest form [62].

3.5. The batch adsorption method of MB adsorption via ZnO NPs

3.5.1. Impact of the pH

Figure 6 Depicts the MB adsorption after 60 min in the dark as well as the percentage of ZnO NPs that degraded as a function of the solutions initial pH. The pH value rose together with the amount of MB adsorbed. The greatest adsorption was 83% for pH values between 7 and 8, with 7.8 being the most efficient pH according to MB, Ji-Zhou Kong et al. [31], who also found that the maximum degradation rate was attained at pH = 8. To be clear, it can be seen that NPs absorbed 61% of MB under acidic conditions in the dark, and then 12% of MB was destroyed under light, resulting in the removal of 73% of MB overall. Similar to this, with pH = 10, the adsorption climbed to 64.5% under darkness, and then 12.5% of the dye was destroyed under light, indicating a total clearance of 77%. At the neutral

condition, the percentages of adsorption and degradation were 83% and 12.2%, respectively, indicating a total removal of 95.2%. This shows that the amount of dye adsorbed increased by roughly 22% as pH increased from 2.0 to above 7.0, whereas the amount of dye dissolved by the sample remained essentially unchanged (~12%). These findings demonstrate that the original solutions pH has a minimal impact on the adsorption process but has no discernible impact on the photocatalytic activity of ZnO NPs [63]. This suggests that the degree of ionization and speciation of the adsorbate, as well as the pH of the solution, all affect the surface charge of the adsorbent. Due to the increased electrostatic attraction between positively charged dye cations and negatively charged adsorption sites caused by the increased availability of negative charge at high pH, dye adsorption will increase.

3.5.2. The dose effect of ZnO NPs on removal degrade percentage of MB dye

Figure 7a Illustrates how the mass ratio of the solid to liquid in the first phase, which is followed by an increase at the quantity of 0.025 g, results in an increase in the MB removal capacity. The uptake of MB from the sorption solution may be explained by the fact that the effective adsorption active sites on

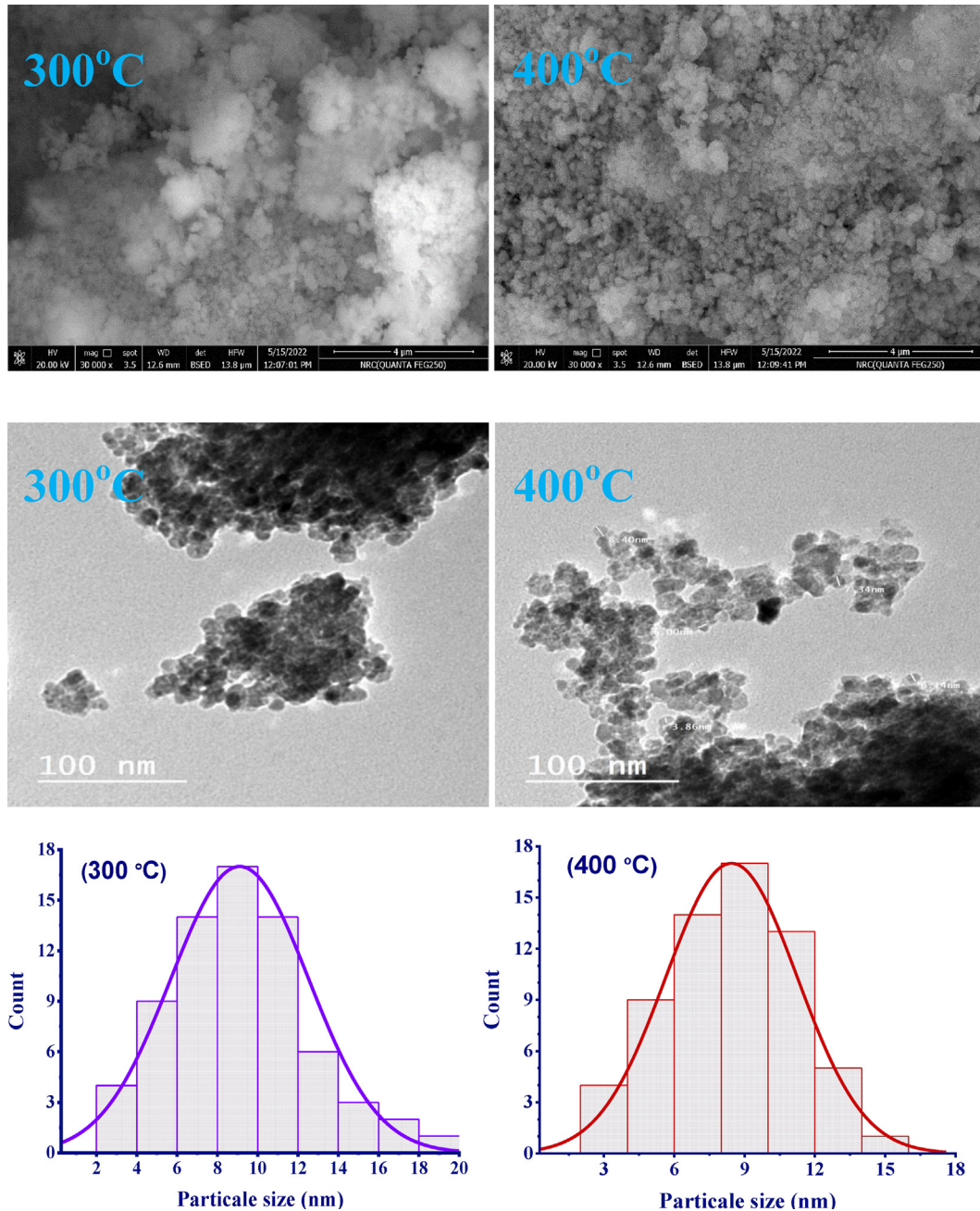


Fig. 4. Particle size distributions, scanning electron microscopy and transmission electron microscopy of fabricated zinc oxide nanoparticles calcined 300 and 400 °C 2 h.

the surface of the nanomaterial significantly raised as the nano-adsorbent dose was increased. However, the dose of nanomaterials increased, the MB dyes absorption efficiency reached the equilibrium level. After this saturation point, every increase in the solid dose will only result in a thickening of the MB adsorbed layer at the adsorbent surface [64] (Fig. 7b) displays the effectiveness of the NPs catalyst in degrading MB. As the amount of catalyst grows, it is clear that the rate of deterioration also

increases significantly. This might be explained by the rise in active sites on the surface brought on by the addition of the 25 mg of NPs catalyst [65].

3.5.3. Effect of initial MB concentration

As shown in (Fig. 8a), as the initial MB concentration increases, so does the MB uptake capability. After exceeding 20 mg/L, the adsorption capacities practically remained unchanged. This could have been brought on by a lack of active sites that could

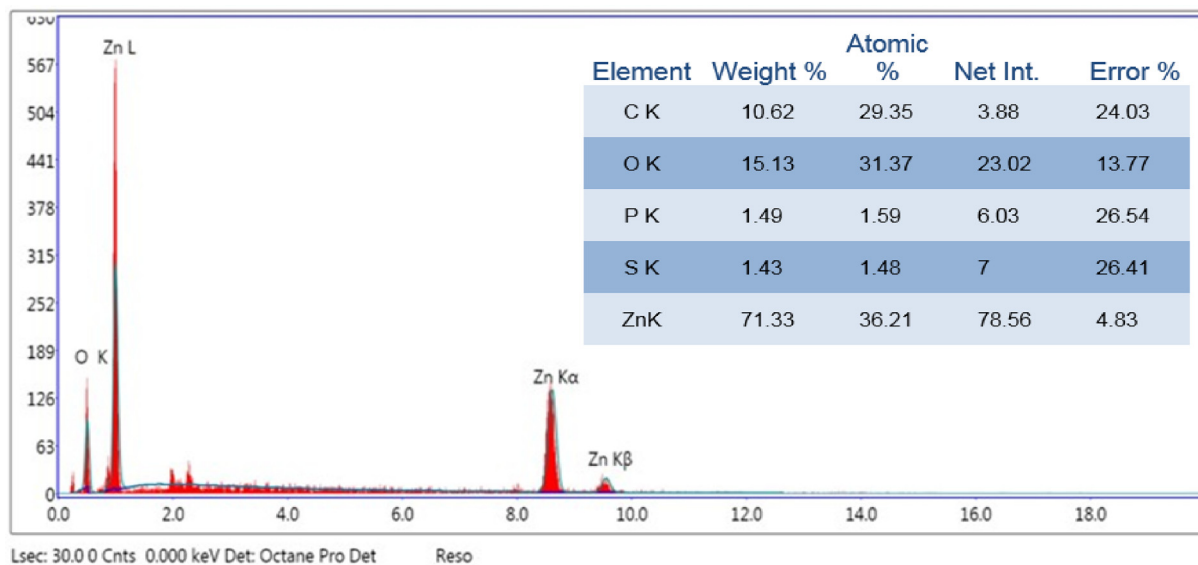


Fig. 5. Energy-dispersive radiography analysis of as-prepared zinc oxide nanoparticles.

accommodate more MB dye. The maximal MB dye adsorption capability of ZnO NPs is 10.04 mg/g. When the MB concentration reached 10 mg/L, the produced nano-adsorbents MB removal percentage, shown in (Fig. 8b), first increased before falling. The rate of MB removal decreases as MB concentration rises because there is inadequate surface area of the nano-adsorbents available for removal during the initial increase in MB concentration. The equilibrium was reached because MB ions bonded to every adsorption site on the surface of the nanomaterials [64].

3.5.4. Isotherm models

Using Langmuir and Freundlich adsorption isotherms, it was determined how MB molecules bind

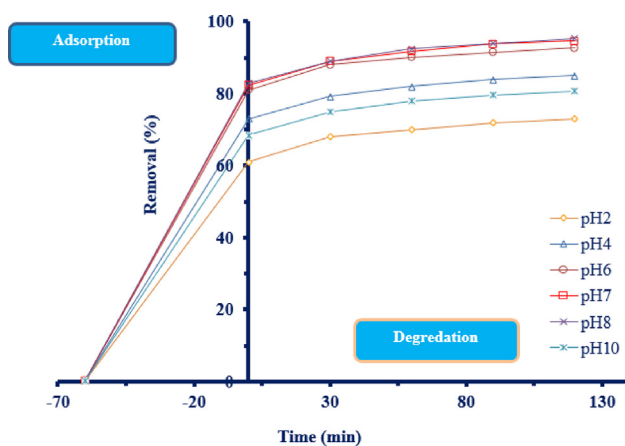


Fig. 6. Under conditions of darkness and visible light irradiation, the pH effected on the adsorption and photocatalytic degradation processes of methylene blue via zinc oxide nanoparticles.

to the produced ZnO NPs throughout the adsorption process (Fig. 9a and b) demonstrates that the adsorption data obtained here was closely related to the Langmuir model, with a higher relation coefficient ($R^2 = 0.9989$) than that found in Table 7 for the Freundlich model ($R^2 = 0.8501$), [66,67]. The sample maximum adsorption capacity was calculated using this isotherm model to be 10.8 mg g^{-1} . Dimensionless separation factor for Langmuir R_L is frequently used to assess how favorable the adsorption process is. For the present work, the value of R_L was determined to be 0.0387, indicating that the adsorption of MB by ZnO NPs is extremely favorable [68].

3.5.5. Kinetic models

ZnO NPs capacity to adsorb MB was evaluated using adsorption kinetics and time-dependent MB concentrations (Fig. 10a, b) and Table 1 demonstrate that the pseudo-second order kinetic model ($R^2 = 0.9993$) performed better in fitting experimental kinetic data than the pseudo-first order ($R^2 = 0.9331$). The MB adsorption capacity was calculated with a pseudo-second order kinetic model to be 10.5 mg g^{-1} , which was comparable to the adsorption capacity found in the Langmuir isotherm (10.8 mg g^{-1}).

The estimated pseudo-second order rate constant is 0.9369 g/mg.min , as shown in Table 8. In the event that a pseudo-second order kinetic model better fits the data, chemical interactions between the adsorbate and the adsorbent are postulated in the adsorption process. A more accurate pseudo-second-order kinetic model in this work demonstrates

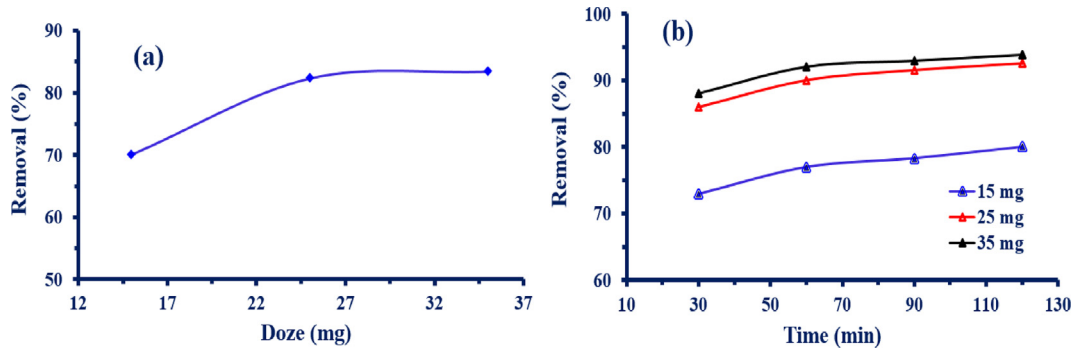


Fig. 7. Influence of amount zinc oxide nanoparticles doses on removal efficiency of methylene blue dye (a), and photocatalytic degradation of methylene blue dye at different doses of zinc oxide nanoparticles (b).

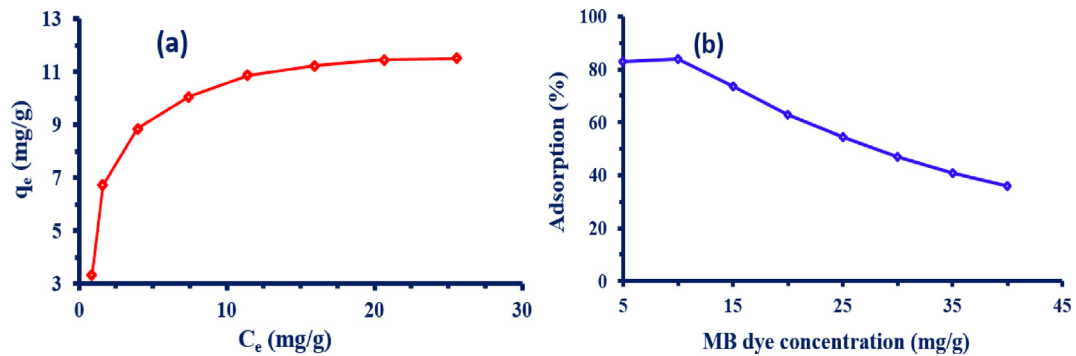


Fig. 8. Adsorption isotherms of methylene blue (a) and effect of initial methylene blue concentration removal onto zinc oxide nanoparticles adsorbent (pH 7.8, adsorbent dose 0.025 g, 1 h) (b).

a possible chemisorption process that may entail valence forces through electron sharing or swapping between MB molecules and ZnO NP surfaces [25].

3.5.6. Photocatalytic degradation of MB at diverse conditions

Fig. 11 explains the photocatalytic degradation of 10.0 mg/L of MB under three different experimental conditions, including UV-alone, UV-catalyst, and

catalyst in the dark. A degradation rate of about 83% was observed because the MB dye was absorbed onto the catalyst NPs surface during the initial 60 min of degradation. A maximum deterioration of 95.2% was reached in 120 min. When evaluated under direct UV light, the degradation rate was found to be 58.3% in 120 min, and it was also discovered to be incredibly low in the same circumstances without a catalyst.

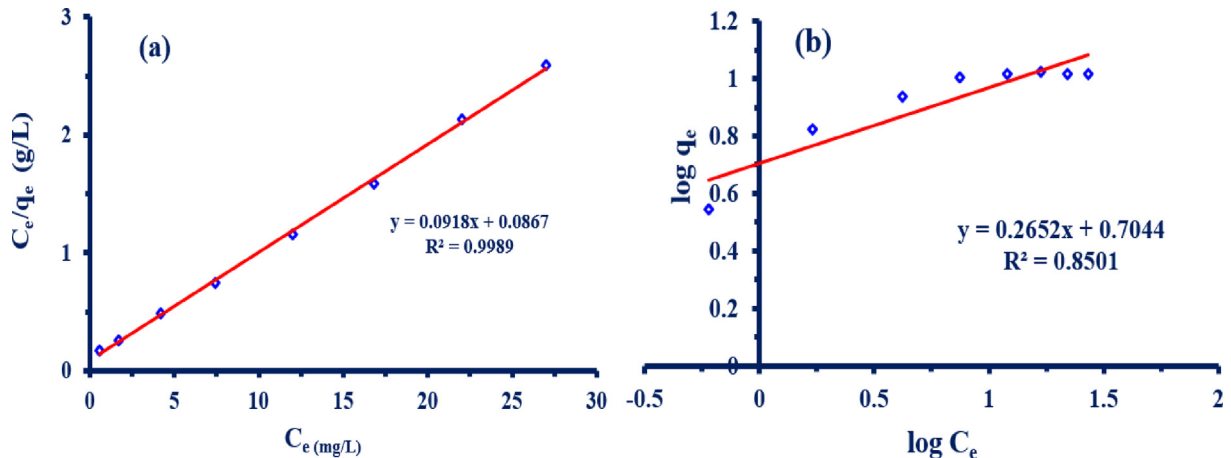


Fig. 9. Plot of C_e/q_e versus C_e for estimation of the Langmuir (a) and plot of $\log q_e$ versus $\log C_e$ for estimation of the Freundlich models (b).

Table 7. The parameters of isotherm models of methylene blue removal via zinc oxide nanoparticles adsorbent.

Adsorbent	Item	Isotherm models			
		Langmuir	Freundlich	Temkin	D-R
ZnO NPs	Model parameter	$q_m = 10.8$ $K_L = 1.05$ $R_L = 0.0387$	$K_F = 5.06$ $n = 3.77$ $1/n = 0.265$	$A_T = 19.8$ $B_T = 1.8$ $b_T = 1.37$	$q_m = 9.97$ $E_D = 1.65$
	R^2	0.9989	0.8501	0.9118	0.9557

The adsorption and degradation behavior. Figure 12 depicts the dyes adsorption and degradation behavior after 60 min in the dark. The remaining trials involved exposing the solutions to visible light (120 min). The adsorption of MB on ZnO NPs increased proportionately with the quantity of MB dye up to 40 mg/L, as is shown from Fig. 12. Initial MB concentrations of 5 and 10 mg/L had the highest adsorption performance of any other substances with roughly 88 and 83%; however, when MB concentration increased, the adsorption capacity decreased to 72, 62.8, 37.5, and 33% for concentrations of 15, 25, 35, and 40 mg/L. However, further raising the concentration of MB had a negative impact on the adsorption procedure, perhaps because fewer MB molecules were able to adsorb to ZnO surfaces [64]. The 'degradation %' of MB concentration as a function of time is also shown in Fig. 12. After 2 h, 95.2% of the dye had been removed from system (12.2% with photocatalysis), followed by 85% (13%), 68% (16%), 53.8% (16.3%), and 47% (14% with photocatalysis) for the dye concentrations of 10, 15, 25, 35, and 40 mg/L, respectively. This demonstrates that around 14% of the dye was lost via the degradation mechanism. Additionally, it was noted that the degradation typically occurred in two stages. A faster stage was followed by a slower stage of photodegradation. In addition to the intermediates that had accumulated in the first stage, the delayed deterioration in the second stage may also be caused by the difficulties in oxidizing the dyes N-atoms [69].

In Fig. 13, the MB concentration appears to be rapidly reduced by adsorption during a period of 60 min, followed by a slow decline in the remaining MB concentration that was practically complete after 120 min. After a 2 h photocatalysis stage, the dark blue solution vanished and the hue of the solution turned clear. According to reports in the literature, it may take up to several hours for ZnO NPs to completely decompose or remove all of the colour molecules. For the current investigation, however, the combination of adsorption and photocatalysis enables the total removal of the pollutant molecules in a reasonable amount of time. This behavior is a result of the samples increased adsorption capacity as well as increased photocatalytic activity brought on by the increased light absorption. Table 9 provides information from recent research that looked at ZnO NPs as effective photocatalysts in the literature.

Table 9 Demonstrates how ZnO NPs photocatalytic action varies greatly in terms of efficiency and duration. This is a predictable outcome given that a number of variables, including the type of model pollutant, the catalysts particle size and surface characteristics, the initial concentration of the dye and catalyst, the source and intensity of the light, and the distance to the light source, can influence the photocatalytic activity. This study's presentation of the ZnO NPs combination adsorption–photocatalytic activity led to a total elimination of 95.2% of the starting dye concentration in 120 min, which is higher than the majority of

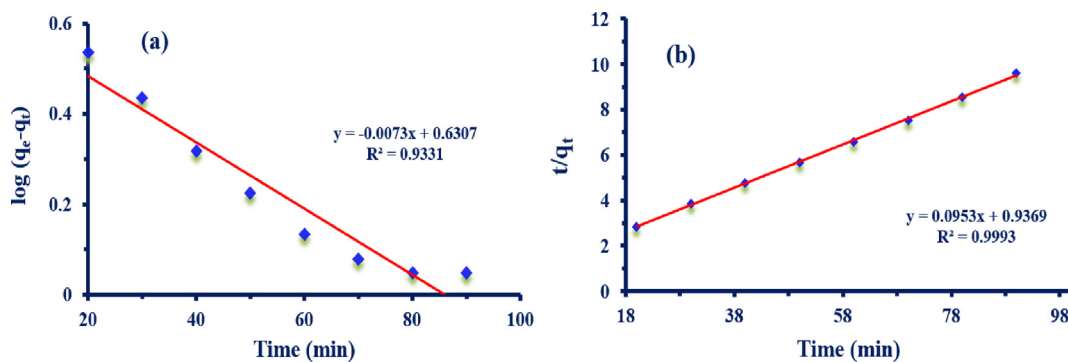


Fig. 10. The kinetic models of pseudo-first (a) and pseudo-second orders, for methylene blue adsorption process via zinc oxide nanoparticles (b).

Table 8. The parameters of kinetic models of methylene blue removal via zinc oxide nanoparticles adsorbent.

Adsorbent	Kinetic models			
	Pseudo-first order	Pseudo-second order	Elovich	Intraparticle diffusion
ZnO NPs	$q_e = 4.2$ $K_1 = 0.0226$ $R^2 = 0.9331$	$q_e = 10.5$ $K_2 = 0.0096$ $R^2 = 0.9993$	$\alpha = 2.08 \times 10^3$ $\beta = 1.28$ $R^2 = 0.9699$	$K_{int} = 5.2$ $C = 0.47$ $R^2 = 0.8237$

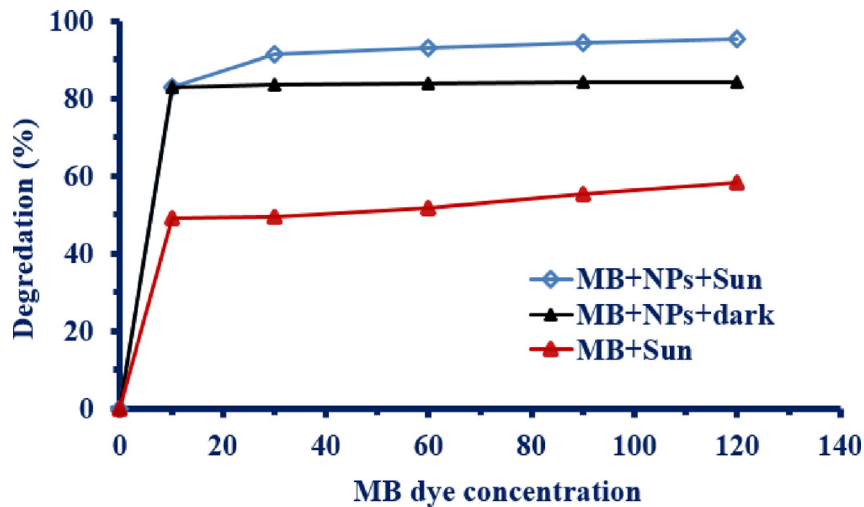


Fig. 11. Degradation of methylene blue by photocatalysis under various experimental conditions (NPs = 0.025 g/L and MB = 10 mg/L).

previously reported values in the literature for similar compositions.

Photodegradation mechanism. The following processes are often guaranteed in the photocatalytic degradation reaction of the MB dye by ZnO NPs: photoexcitation, charge separation and migration, and finally surface oxidation–reduction reactions, as shown in Fig. 14. Conduction band electrons (e^-) and valence band holes (h^+) were produced on the catalyst's surface when the ZnO NPs were exposed

to sunlight. While oxygen produced superoxide radical anion ($\cdot O_2^-$), the holes produced extremely reactive hydroxyl radicals ($\cdot OH$) when they reacted with water [18,71]. As a result, the ZnO NPs huge surface area and mesoscopic nature produced exceptional photocatalytic activity, which may have a significant impact on the creation of photocatalysts for the removal of organic contaminants from wastewater.

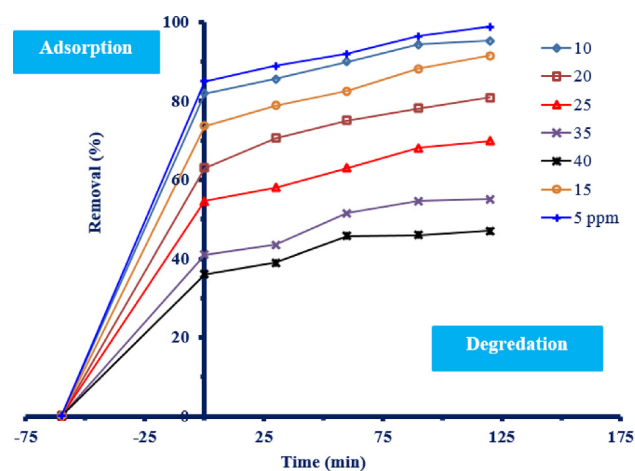


Fig. 12. The adsorption and degradation behavior of the methylene blue dye removal via zinc oxide nanoparticles.

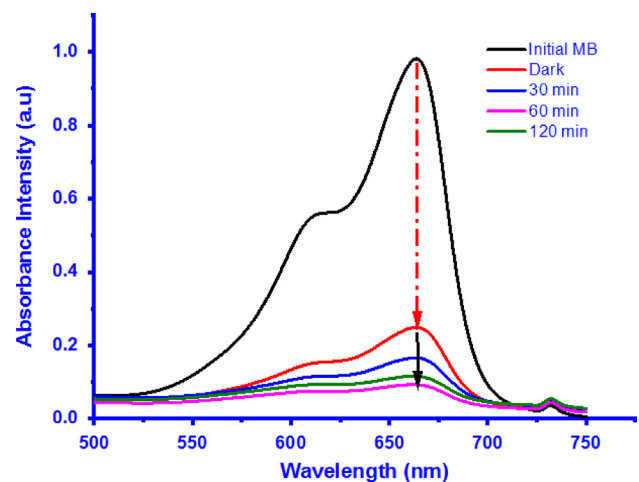


Fig. 13. Absorption spectra of methylene blue solutions treated by zinc oxide nanoparticles.

Table 9. Comparative analysis of photocatalytic degradation of methylene blue dye via zinc oxide nanoparticles.

Plant source	Salt	Size (nm)	Initial conc. of MB dye	Doze of adsorbent	Light source	Degradation efficiency % (time)	Reference
<i>Mussaenda frondosa</i>	Zinc nitrate	5–20	5 mL/5 ppm	20 mg	UV	80%-100 min 30%-100 min	[51]
<i>Sambucus ebulus</i>	Zinc acetate	17	50 ppm	20 mg	UV	80%-200 min	[52]
<i>C. sinensis</i>	Zinc nitrate	22.6	15 ppm	200 mg	UV	83%-120 min	[53]
<i>Brassica oleracea L. var. italica</i>	Zinc chloride	14–17	25 mL/5 × 10 ⁻⁵ M	20 mg	UV	74%-180 min	[7]
<i>Tabernaemontana divaricata</i>	Zinc nitrate	20–50	25 mL/5 × 10 ⁻⁵ M	100 mg	Sunlight	100%-90 min	[55]
<i>Azadirachta indica</i>	Zinc nitrate	9–38	10 ppm	60 mg	Sunlight	85–120 min	[57]
<i>Calliandra aematocephala</i>	Zinc acetate	19.45	20 ppm	50 mg	Sunlight	88%-270 min	[38]
<i>Ziziphus jujuba</i>	Zinc acetate	25 nm	20 mL/5 ppm	15 mg	Solar radiation	99% -120 min	[69]
Fresh green leaves	Zinc sulfate	40–50	100 mL/10 ppm	20 mg	Sunlight	94%-150 min	[70]
Onion extract	Zinc sulfate	2–15	20 mL/10 ppm	25 mg	Sunlight	95.2%-120 min	This study

3.5.7. The antimicrobial activity of ZnO NPs

The values of the minimum inhibitory concentration were assessed to study the antibacterial characteristics of the biosynthesis of ZnO NPs using red onion extract. The results are shown in Table 10 below. Following treatment with ZnO NPs at various concentrations 225, 250, 275, and 300 µg/mL against *S.typhimurium* and *E.coli*, *E.faecalis*, and *S.aureus*, the antibacterial activity demonstrated inhibitory zones (Gram-positive bacteria). Against both Gram-positive and Gram-negative bacteria, the ZnO NPs showed strong antibacterial action, according to the antibacterial activity results. *S. typhimurium*, *E. coli*, *S. aureus*, and *E. faecalis* growth inhibition has generally been increased by increasing the concentration of ZnO NPs. The zone of inhibition that ZnO NPs create against all different microbes is depicted in Figs. 15 and 16. *E. coli* (MIC 31.2 ± 0.76 mm), *S. aureus* (MIC

Table 10. Evaluation the antibacterial activity of zinc oxide nanoparticles (mean ± standard deviation; n = 3).

Microorganisms	Gram reactive	ZnO NPs		Ciprofloxacin
		25 µL from 250 µg/mL	25 µL from 275 µg/mL	
Inhibition zone (mm)				
<i>E.coli</i>	- ve	31.2 ± 0.76	30.5 ± 0.50	
<i>S.aureus</i>	+ ve	30.2 ± 1.04	30.3 ± 0.58	
<i>E. faecalis</i>	+ ve	28.3 ± 0.76	28.1 ± 0.76	
<i>S. typhimurium</i>	- ve	26.0 ± 0.94	30.6 ± 0.47	

30.2 ± 1.04 mm), *E. faecalis* (MIC 28.3 ± 0.76 mm), and *S. typhimurium* (MIC 26.3 ± 0.94 mm) were shown to be the species most sensitive to the nanoparticles. Therefore, as compared with conventional antibiotics, ZnO NPs showed better antibacterial activity against gram-negative (*E. coli*) than gram-positive (*S. aureus*) bacteria. This is in line with earlier research that found ZnO NPs had a larger



Fig. 14. The suggested process for how zinc oxide nanoparticles photodegrade methylene blue dye.

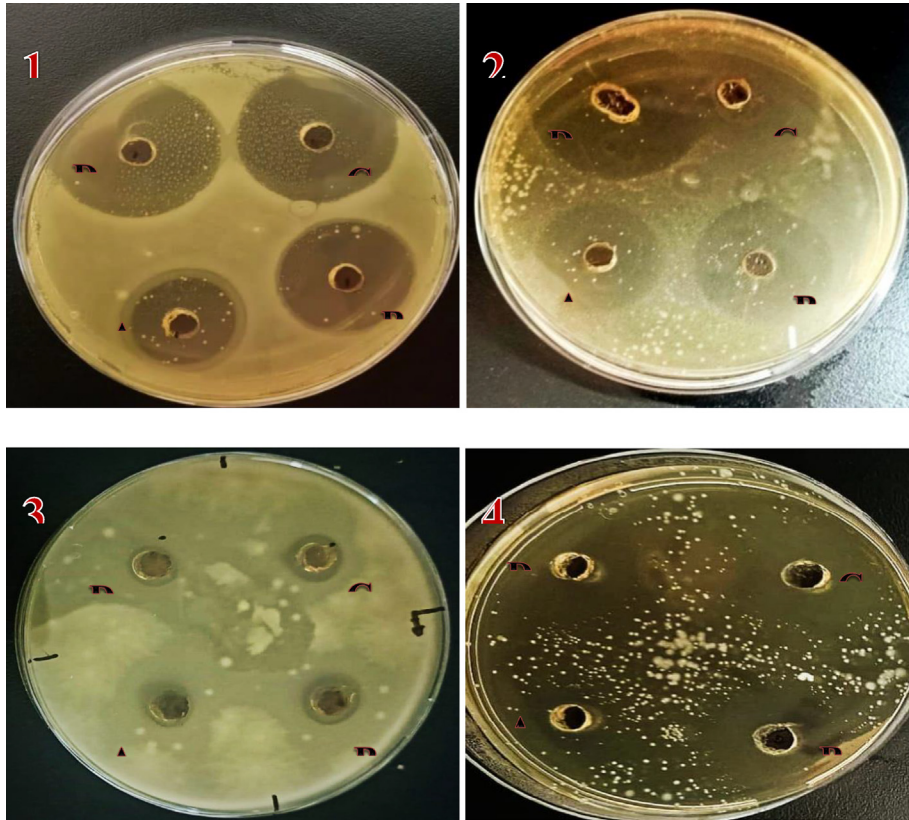


Fig. 15. The effect of zinc oxide nanoparticles against; (1) *E.coli* (2) *S. aureus* (3) *E. faecalis* (4) *S. typhimurium* for representing bacteria. The concentration of solutions, A = 225, B = 250, C = 275, and D = 300 $\mu\text{g/mL}$.

antibacterial effect on gram-negative bacteria than gram-positive bacteria [72]. However, it has been found that ZnO NPs have a stronger effect on gram-positive bacteria than gram-negative bacteria. This argument emphasizes the significance of comprehending the mechanism underlying ZnO NPs antibacterial action. Additionally, the efficiency of the functional groups that helped produce ZnO NPs during their biogenesis. Previous studies have described the mechanism of ZnO NPs antimicrobial

activity, and they claimed that ZnO NPs exhibit antimicrobial activity by damaging cell membranes as a result of direct or electrostatic contact between ZnO NPs and cell surfaces, cellular internalization of ZnO NPs, and the production of active oxygen species like H_2O_2 in cells as a result of metal oxides [73].

Figure 17 Shows a comparison of 25 μL of (250 $\mu\text{g/mL}$) ZnO NPs, 25 μL of (275 $\mu\text{g/mL}$) *Ciprofloxacin*, DMSO, and onion extract. In the inhibition zone

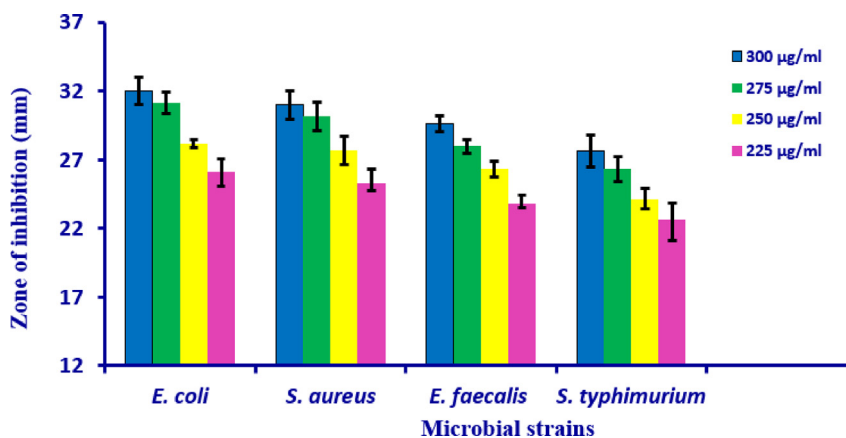


Fig. 16. The antibacterial activities of zinc oxide nanoparticles, *E.coli*, *S.aureus*, *E. faecalis*, and *S.typhimurium*.

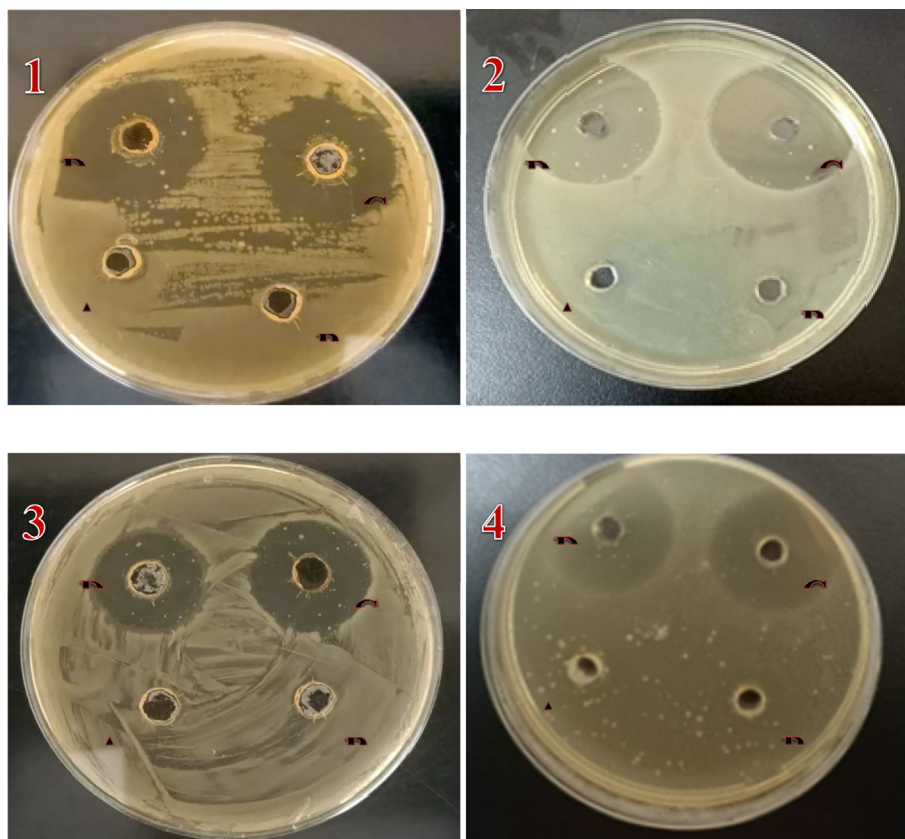


Fig. 17. The antimicrobial activity of 250 µg/mL zinc oxide nanoparticles against (1) *E. coli* (2) *S. aureus* (3) *E. faecalis*, and *S. typhimurium* (4), the letters A, B, C, and D refer to DMSO and onion extract, 250 µg/mL zinc oxide nanoparticles and 275 µg/mL of Ciprofloxacin, respectively.

that was visible from each plate, the data demonstrated that the biosynthesized ZnO NPs worked better than the *Ciprofloxacin* employed as a positive control, but there was no inhibition zone in the controlled wells treated with red onion extract and DMSO. The highest inhibitory zone against *E. coli* and *S. aureus* was seen, and it was followed by *E. faecalis* and *S. typhimurium*, showing that the bacteria were more averse to nanoparticle production. ZnO NPs may be more successful at inactivating a human infections than regular antibiotics, according to the antibacterial activity, which demonstrated that they are more harmful to bacterial cells.

3.6. Conclusions

The biosynthesis of ZnO NPs using red onion extract was the main focus of our study, and we also looked at how well these NPs removed the MB dye from water using adsorption-photocatalysis procedures as well as their antibacterial activities. The phytoconstituents play a major role in the synthesis of NPs, as evidenced by the presence of these compounds in FT-IR analyses for both aqueous onion extract and ZnO NPs. The XRD results

showed that the hexagonal wurtzite structure of ZnO NPs was what all of the measured peak intensity profiles were. According to SEM and TEM examinations, the ZnO NPs had a spherical form, a cluster of agglomerated particles, and a particle size range of 2.83–15.35 nm. The elemental compositions of the ZnO NPs were validated by the EDX analysis. NPs demonstrated the greatest outcomes for the photocatalytic and adsorption processes used to remove MB dye. The best removal efficiency for the adsorption and degradation process was pH = 7.8. The effectiveness of the procedure diminishes as the dye concentration of the MB in the process rises, as shown by altering the dye concentration from 10 to 40 mg/L. When using NPs photocatalyst at a dosage of 25 mg/L and a dye concentration of 10 mg/L, the degradation of dye efficiency was at its highest. The results of the adsorption investigations indicated that the Langmuir isothermal model, with a maximum adsorption capacity of 10.8 mg/g and $R^2 = 0.9989$, was the most appropriate one. On the other hand, the kinetic analysis supported the adsorption reactions pseudo-second-order behavior. Overall, the results showed that the photocatalytic and adsorption

approaches removed the dye up to 95.2% more efficiently than in earlier research, resulting in the most environmentally beneficial system. The bio-produced ZnO NPs were also applied for antimicrobial purposes. The ZnO NPs appeared to have a more toxic effect on bacterial cells, and they may also be more effective at inactivating some human pathogens than the conventional antibiotic *Ciprofloxacin*, according to the antimicrobial activity.

Conflicts of interest

The authors declare no conflict of interest.

References

- [1] Reinsch H. Green Synthesis of metal-organic frameworks. *Eur J Inorg Chem* 2016;2016:4290–9.
- [2] Ali I, Alharbi OML, Allothman ZA, Badjah AY, Alwarthan A, Basheer AA. Artificial neural network modelling of amido black dye sorption on iron composite nano material: kinetics and thermodynamics studies. *J Mol Liq* 2018;250:1–8.
- [3] Gour A, Jain NK. Advances in green synthesis of nanoparticles. *Artif Cell Nanomed Biotechnol* 2019;47:844–51.
- [4] Abbasi BA, Iqbal J, Ahmad R, Zia L, Kanwal S, Mahmood T, et al. Bioactivities of Geranium wallichianum leaf extracts conjugated with zinc oxide nanoparticles. *Biomolecules* 2019; 10:38.
- [5] Al-Hakkani MF, Gouda GA, Hassan SH. A review of green methods for phyto-fabrication of hematite (α -Fe₂O₃) nanoparticles and their characterization, properties, and applications. *Heliyon* 2021;7:e05806.
- [6] El Shafey AM. Green synthesis of metal and metal oxide nanoparticles from plant leaf extracts and their applications: a review. *Green Process Synth* 2020;9:304–39.
- [7] Osuntokun J, Onwudiwe DC, Ebenso EE. Green synthesis of ZnO nanoparticles using aqueous Brassica oleracea L. var. italica and the photocatalytic activity. *Green Chem Lett Rev* 2019;12:444–57.
- [8] Becheri A, Dürr M, Lo Nostro P, Baglioni P. Synthesis and characterization of zinc oxide nanoparticles: application to textiles as UV-absorbers. *J Nanoparticle Res* 2008;10:679–89.
- [9] Zhang Z-Y, Xiong H-M. Photoluminescent ZnO nanoparticles and their biological applications. *Materials* 2015;8: 3101–27.
- [10] Singh J, Kaur S, Kaur G, Basu S, ZnO nanoparticles Rawat M Biogenic. A study of blueshift of optical band gap and photocatalytic degradation of reactive yellow 186 dye under direct sunlight. *Green Process Synth* 2019;8:272–80.
- [11] Shashanka R, Esgin H, Yilmaz VM, Caglar Y. Fabrication and characterization of green synthesized ZnO nanoparticle based dye-sensitized solar cells. *J Sci Adv Mater Dev* 2020;5:185–91.
- [12] Singh TA, Das J, Sil PC. Zinc oxide nanoparticles: a comprehensive review on its synthesis, anticancer and drug delivery applications as well as health risks. *Adv Colloid Interface Sci* 2020;286:102317.
- [13] Varadavenkatesan T, Lyubchik E, Pai S, Pugazhendhi A, Vinayagam R, Selvaraj R. Photocatalytic degradation of Rhodamine B by zinc oxide nanoparticles synthesized using the leaf extract of *Cyanometra ramiflora*. *J Photochem Photobiol, B* 2019;199:111621.
- [14] Ong CB, Ng LY, Mohammad AW. A review of ZnO nanoparticles as solar photocatalysts: synthesis, mechanisms and applications. *Renew Sustain Energy Rev* 2018;81:536–51.
- [15] Wang ZL. Zinc oxide nanostructures: growth, properties and applications. *J Phys Condens Matter* 2004;16:R829.
- [16] Abdulhadi A S, A Gouda G, Hamed A M, Abu-Saied M, El-Mottaleb M. Synthesis of zno nano powders using polyethylene glycol by the controlled microwave method. *Bull Pharmac Sci Assiut* 2022;45:23–40.
- [17] Ahmed E-SA, El-Sayed BA, Mohamed WA, Fahmy A, Helal A. Recycling of supported nanocomposites for hazardous industrial wastewater treatment via Solar photocatalytic process. *Egypt J Pet* 2021;30:29–35.
- [18] Pung S-Y, Lee W-P, Aziz A. Kinetic study of organic dye degradation using ZnO particles with different morphologies as a photocatalyst. *Int J Inorg Chem* 2012;2012, 9 pages.
- [19] Mohamed WA, Fahmy A, Helal A, Ahmed EA, Elsayed BA, Kamoun EA, et al. Degradation of local Brilliant Blue R dye in presence of polyvinylidene fluoride/MWCNTs/TiO₂ as photocatalysts and plasma discharge. *J Environ Chem Eng* 2022;10:106854.
- [20] Fahmy A, El-Zomrawy A, Saeed AM, Sayed AZ, El-Arab MAE, Shehata HA. Modeling and optimizing Acid Orange 142 degradation in aqueous solution by non-thermal plasma. *Chemosphere* 2018;210:102–9.
- [21] Ullah R, Dutta J. Photocatalytic degradation of organic dyes with manganese-doped ZnO nanoparticles. *J Hazard Mater* 2008;156:194–200.
- [22] Fahmy A, El-Zomrawy A, Saeed AM, Sayed AZ, El-Arab MAE, Shehata H, et al. Degradation of organic dye using plasma discharge: optimization, pH and energy. *Plasma Res Express* 2020;2:015009.
- [23] Al-Hakkani MF, Gouda GA, Hassan SH, Saddik MS, El-Mokhtar MA, Ibrahim MA, et al. Cefotaxime removal enhancement via bio-nanophotocatalyst α -Fe₂O₃ using photocatalytic degradation technique and its echo-biomedical applications. *Sci Rep* 2022;12:1–20.
- [24] Lim WY, Wu H, Lim Y-F, Ho GW. Facilitating the charge transfer of ZnMoS₄/CuS p–n heterojunctions through ZnO intercalation for efficient photocatalytic hydrogen generation. *J Mater Chem A* 2018;6:11416–23.
- [25] Dursun S, Kaya İC, Kocabaş M, Akyıldız H, Kalem V. Visible light active heterostructured photocatalyst system based on CuO plate-like particles and SnO₂ nanofibers. *Int J Appl Ceram Technol* 2020;17:1479–89.
- [26] Javier Moreno F, Corzo-Martónez M, Dolores del Castillo M, Villamiel M. Changes in antioxidant activity of dehydrated onion and garlic during storage. *Food Res Int* 2006;39:891–7.
- [27] Momoh JO, Manuwa AA, Ayinde FA, Bankole YO. Nutritional, phytochemicals, GC-MS and antibacterial activities of aqueous red onion (*Allium cepa*) extract against *Staphylococcus aureus* and *Escherichia coli*. *Int J Trop Dis Health* 2023;44:35–51.
- [28] Lu X, Wang J, Al-Qadiri HM, Ross CF, Powers JR, Tang J, et al. Determination of total phenolic content and antioxidant capacity of onion (*Allium cepa*) and shallot (*Allium oschaninii*) using infrared spectroscopy. *Food Chem* 2011;129:637–44.
- [29] Hassanien R, Husein DZ, Khamis M. Novel green route to synthesize cadmium oxide@graphene nanocomposite: optical properties and antimicrobial activity. *Mater Res Express* 2019;6:085094.
- [30] Ramesh P, Saravanan K, Manogar P, Johnson J, Vinoth E, Mayakannan M. Green synthesis and characterization of biocompatible zinc oxide nanoparticles and evaluation of its antibacterial potential. *Sens Bio-Sens Res* 2021;31:100399.
- [31] Kong J-Z, Li A-D, Li X-Y, Zhai H-F, Zhang W-Q, Gong Y-P, et al. Photo-degradation of methylene blue using Ta-doped ZnO nanoparticle. *J Solid State Chem* 2010;183:1359–64.
- [32] Sayed AS, Abdelmottaleb M, Cheira MF, Abdel-Aziz G, Gomaa H, Hassanein TF. Date seed as an efficient, eco-friendly, and cost-effective bio-adsorbent for removal of thorium ions from acidic solutions. *Aswan Uni J Environ Stud* 2020;1:106–24.
- [33] Al-Hakkani MF, Gouda GA, Hassan SH, Mohamed MM, Nagiub AM. Cefixime wastewater management via bio-engineered Hematite nanoparticles and the in-vitro synergistic potential multifunction activities of Cefixime@Hematite nanosystem. *Surface Interfac* 2022;30:101877.

- [34] Hassan R, Gahlan A, Gouda GA, Aly-Eldeen MA-E, Badawy N. Development of zinc removal process from contaminated water using statistical approaches. *Egypt J Chem* 2022;65:1099–110.
- [35] Ho Y-S, McKay G. Pseudo-second order model for sorption processes. *Process Biochem* 1999;34:451–65.
- [36] Liang S, Guo X, Feng N, Tian Q. Isotherms, kinetics and thermodynamic studies of adsorption of Cu²⁺ from aqueous solutions by Mg²⁺/K⁺ type orange peel adsorbents. *J Hazard Mater* 2010;174:756–62.
- [37] Al-Khateeb LA, Hakami W, Salam MA. Removal of non-steroidal anti-inflammatory drugs from water using high surface area nanographene: kinetic and thermodynamic studies. *J Mol Liq* 2017;241:733–41.
- [38] Vinayagam R, Selvaraj R, Arivalagan P, Varadavenkatesan T. Synthesis, characterization and photocatalytic dye degradation capability of Calliandra haematocephala-mediated zinc oxide nanoflowers. *J Photochem Photobiol, B* 2020;203:111760.
- [39] Wahab R, Hwang I, Kim Y-S, Musarrat J, Siddiqui M, Seo H-K, et al. Non-hydrolytic synthesis and photo-catalytic studies of ZnO nanoparticles. *Chem Eng J* 2011;175:450–7.
- [40] Rahman QI, Ahmad M, Misra SK, Lohani M. Effective photocatalytic degradation of rhodamine B dye by ZnO nanoparticles. *Mater Lett* 2013;91:170–4.
- [41] Ameri M, Raoufi M, Zamani-Meymian M-R, Samavat F, Fathollahi M-R, Mohajerani E. Self-assembled ZnO nanosheet-based spherical structure as photoanode in dye-sensitized solar cells. *J Electron Mater* 2018;47:1993–9.
- [42] Al-Farhan BS, Gouda GA, Farghaly O, Khalafawy A. Potentiometric study of new Schiff base complexes bearing morpholine in ethanol-water medium with some metal ions. *Int J Electrochem Sci* 2019;14:3350–62.
- [43] Mustapha T, Ithnin NR, Othman H, Abu Hasan Z-I, Misni N. Bio-fabrication of silver nanoparticles using Citrus aurantifolia fruit peel extract (CAFPE) and the role of plant extract in the synthesis. *Plants* 2023;12:1648.
- [44] Rajiv P, Rajeshwari S, Venkatesh R. Bio-Fabrication of zinc oxide nanoparticles using leaf extract of Parthenium hysterophorus L. and its size-dependent antifungal activity against plant fungal pathogens. *Spectrochim Acta, Part A* 2013;112:384–7.
- [45] Durmus Z, Kurt BZ, Durmus A. Synthesis and characterization of graphene oxide/zinc oxide (GO/ZnO) nanocomposite and its utilization for photocatalytic degradation of basic fuchsin dye. *Chem Select* 2019;4:271–8.
- [46] Gadallah A-S, El-Nahass M. Structural, optical constants and photoluminescence of ZnO thin films grown by sol-gel spin coating. *Adv Condens Matter Phys* 2013;2013, 9 pages.
- [47] Hosny S, Gouda GA, Abu-El-Wafa SM. Novel nano copper complexes of a new Schiff base: green synthesis, a new series of solid Cr (II), Co (II), Cu (II), Pd (II) and Cd (II) chelates, characterization, DFT, DNA, antitumor and molecular docking studies. *Appl Organomet Chem* 2022;36:e6627.
- [48] Elshazly EH, Nasr A, Elnosary ME, Gouda GA, Mohamed H, Song Y. Identifying the anti-MERS-CoV and anti-HCoV-229E potential drugs from the Ginkgo biloba leaves extract and its eco-friendly synthesis of silver nanoparticles. *Molecules* 2023;28:1375.
- [49] Elshazly EH, Mohamed AKS, Aboelmagd HA, Gouda GA, Abdallah MH, Ewais EA, et al. Phytotoxicity and antimicrobial activity of green synthesized silver nanoparticles using Nigella sativa seeds on wheat seedlings. *J Chem* 2022;2022, 9 pages.
- [50] Aminuzzaman M, Ying LP, Goh W-S, Watanabe A. Green synthesis of zinc oxide nanoparticles using aqueous extract of *Garcinia mangostana* fruit pericarp and their photocatalytic activity. *Bull Mater Sci* 2018;41:1–10.
- [51] Jayappa MD, Ramaiah CK, Kumar MAP, Suresh D, Prabhu A, Devasya RP, et al. Green synthesis of zinc oxide nanoparticles from the leaf, stem and in vitro grown callus of *Mussaenda frondosa* L.: characterization and their applications. *Appl Nanosci* 2020;10:3057–74.
- [52] Alamdari S, Sasani Ghamsari M, Lee C, Han W, Park H-H, Tafreshi MJ, et al. Preparation and characterization of zinc oxide nanoparticles using leaf extract of *Sambucus ebulus*. *Appl Sci* 2020;10:3620.
- [53] Luque P, Soto-Robles C, Nava O, Gomez-Gutierrez C, Castro-Beltran A, Garrafa-Galvez H, et al. Green synthesis of zinc oxide nanoparticles using Citrus sinensis extract. *J Mater Sci Mater Electron* 2018;29:9764–70.
- [54] Sorbiun M, Shayegan Mehr E, Ramazani A, Taghavi Fardood S. Green synthesis of zinc oxide and copper oxide nanoparticles using aqueous extract of oak fruit hull (Jaft) and comparing their photocatalytic degradation of basic violet 3. *Int J Environ Res Publ Health* 2018;12:29–37.
- [55] Raja A, Ashokkumar S, Marthandam RP, Jayachandiran J, Khatiwada CP, Kaviyarasu K, et al. Eco-friendly preparation of zinc oxide nanoparticles using *Tabernaemontana divaricata* and its photocatalytic and antimicrobial activity. *J Photochem Photobiol, B* 2018;181:53–8.
- [56] Khasay MH, Tadesse A, RamaDevi D, Belachew N, Basavaiah K. Green synthesis of zinc oxide nanostructures and investigation of their photocatalytic and bactericidal applications. *RSC Adv* 2019;9:36967–81.
- [57] Madan H, Sharma S, Suresh D, Vidya Y, Nagabhushana H, Rajanaik H, et al. Facile green fabrication of nanostructure ZnO plates, bullets, flower, prismatic tip, closed pine cone: their antibacterial, antioxidant, photoluminescent and photocatalytic properties. *Spectrochim Acta, Part A* 2016;152:404–16.
- [58] Chauhan A, Verma R, Kumari S, Sharma A, Shandilya P, Li X, et al. Photocatalytic dye degradation and antimicrobial activities of Pure and Ag-doped ZnO using Cannabis sativa leaf extract. *Sci Rep* 2020;10:1–16.
- [59] Shayegan Mehr E, Sorbiun M, Ramazani A, Taghavi Fardood S. Plant-mediated synthesis of zinc oxide and copper oxide nanoparticles by using ferulago angulata (schlecht) boiss extract and comparison of their photocatalytic degradation of Rhodamine B (RhB) under visible light irradiation. *J Mater Sci Mater Electron* 2018;29:1333–40.
- [60] Rupa EJ, Kaliraj L, Abid S, Yang D-C, Jung S-K. Synthesis of a zinc oxide nanoflower photocatalyst from sea buckthorn fruit for degradation of industrial dyes in wastewater treatment. *Nanomaterials* 2019;9:1692.
- [61] Khalafi T, Buazar F, Ghanemi K. Phycosynthesis and enhanced photocatalytic activity of zinc oxide nanoparticles toward organosulfur pollutants. *Sci Rep* 2019;9:1–10.
- [62] Khamis M, Gouda GA, Naguib AM. Biosynthesis approach of zinc oxide nanoparticles for aqueous phosphorous removal: physicochemical properties and antibacterial activities. *BMC Chem* 2023;17:99.
- [63] Cinar B, Kerimoglu I, Tonbul B, Demirbuken A, Dursun S, Kaya IC, et al. Hydrothermal/electrospinning synthesis of CuO plate-like particles/TiO₂ fibers heterostructures for high-efficiency photocatalytic degradation of organic dyes and phenolic pollutants. *Mater Sci Semicond Process* 2020;109:104919.
- [64] Husein DZ, Hassanien R, Khamis M. Cadmium oxide nanoparticles/graphene composite: synthesis, theoretical insights into reactivity and adsorption study. *RSC Adv* 2021;11:27027–41.
- [65] Anantha M, Olivera S, Hu C, Jayanna B, Reddy N, Venkatesh K, et al. Comparison of the photocatalytic, adsorption and electrochemical methods for the removal of cationic dyes from aqueous solutions. *Environ Technol Innovat* 2020;17:100612.
- [66] Hassan E, Gahlan AA, Gouda GA. Biosynthesis approach of copper nanoparticles, physicochemical characterization, cefixime wastewater treatment, and antibacterial activities. *BMC Chem* 2023;17:1–20.
- [67] Al-Hakkani MF, Gouda GA, Hassan SH, Mohamed M, Naguib AM. Environmentally azithromycin pharmaceutical wastewater management and synergetic biocompatible approaches of loaded azithromycin@ hematite nanoparticles. *Sci Rep* 2022;12:1–21.
- [68] Al-Hakkani MF, Gouda GA, Hassan SH, Naguib AM. Echinacea purpurea mediated hematite nanoparticles (α -HNPs) biofabrication, characterization, physicochemical properties,

- and its in-vitro biocompatibility evaluation. *Surface Interfac* 2021;24:101113.
- [69] Alharthi MN, Ismail I, Bellucci S, Khadry NH, Abdel Salam M. Biosynthesis microwave-assisted of zinc oxide nanoparticles with ziziphus jujuba leaves extract: characterization and photocatalytic application. *Nanomaterials* 2021;11:1682.
- [70] Vasantharaj S, Sathiyavimal S, Senthilkumar P, Kalpana V, Rajalakshmi G, Alsehli M, et al. Enhanced photocatalytic degradation of water pollutants using bio-green synthesis of zinc oxide nanoparticles (ZnO NPs). *J Environ Chem Eng* 2021;9:105772.
- [71] Tripathy N, Ahmad R, Kuk H, Hahn Y-B, Khang G. Mesoporous ZnO nanoclusters as an ultra-active photocatalyst. *Ceram Int* 2016;42:9519–26.
- [72] Shaban M, Mohamed F, Abdallah S. Production and characterization of superhydrophobic and antibacterial coated fabrics utilizing ZnO nanocatalyst. *Sci Rep* 2018;8: 1–15.
- [73] Karthik K, Dhanuskodi S, Gobinath C, Sivaramkrishnan S. Microwave-assisted synthesis of CdO–ZnO nanocomposite and its antibacterial activity against human pathogens. *Spectrochim Acta, Part A* 2015;139:7–12.